

Reversible Ir-based multifunctional electrocatalyst for durable water splitting and fuel cell systems

Woong Hee Lee

Korea Institute of Science and Technology

Young-Jin Ko

Korea Institute of Science and Technology

Jung Hwan Kim

Yonsei University

Chang Hyuck Choi

Gwangju Institute of Science and Technology <https://orcid.org/0000-0002-2231-6116>

Keun Hwa Chae

Korea Institute of Science and Technology <https://orcid.org/0000-0003-3894-670X>

Hansung Kim

Yonsei University

Yun Jeong Hwang

Korea Institute of Science and Technology <https://orcid.org/0000-0002-0980-1758>

Byoung Koun Min

Korea Institute of Science and Technology <https://orcid.org/0000-0001-5766-0251>

Peter Strasser

Technical University of Berlin <https://orcid.org/0000-0002-3884-436X>

Hyung-Suk Oh (✉ hyung-suk.oh@kist.re.kr)

Korea Institute of Science and Technology <https://orcid.org/0000-0002-0310-6666>

Article

Keywords: Hydrogen evolution reaction (HER), Oxygen evolution reaction (OER), Hydrogen oxidation reaction (HOR), Reversible multifunctional electrocatalyst, Iridium, H₂ fuel starvation, Voltage reversal

Posted Date: September 10th, 2020

DOI: <https://doi.org/10.21203/rs.3.rs-66651/v1>

License: © ⓘ This work is licensed under a Creative Commons Attribution 4.0 International License.

[Read Full License](#)

Abstract

The voltage reversal of water electrolyzers and fuel cells induces a large positive potential on the hydrogen electrodes, followed by severe system degradation. Applying a reversible multifunctional electrocatalyst to the hydrogen electrode is a practical solution. Ir exhibits excellent catalytic reactivity for hydrogen evolution reactions (HER), and hydrogen oxidation reactions (HOR) around 0 V/RHE, yet irreversibly converts to amorphous IrO_x at potentials > 0.8 V/RHE, which is an excellent catalyst for oxygen evolution reactions (OER), yet a poor HER and HOR catalyst. Harnessing these multifunctional catalytic characteristics, we designed a unique Ir-based electrocatalyst for OER, HER, and HOR. Under OER operation, the crystalline nanoparticle catalyst generates an atomically-thin, highly active IrO_x layer, which reversibly transforms into a metallic Ir surface at more cathodic electrode potentials, restoring high catalytic activity for HER and HOR. Our analysis reveals that a metallic Ir subsurface to the thin IrO_x surface layer can act as a catalytic substrate for the reduction of the dissolved Ir ion, creating reversibility. Our work not only uncovers new fundamental, uniquely reversible catalytic properties of nanoparticle catalysts, but also offers a practical materials-based solution to catalyst layer degradation of electrochemical energy conversion devices.

Background

In view of a clean and renewable society, there has been great interest in water electrolysis and fuel cells for producing and using hydrogen, which is considered a promising energy carrier^{1,2}. Water electrolysis consists of a two-electrode reaction: a hydrogen evolution reaction (HER) and an oxygen evolution reaction (OER)^{3,4}. Fuel cells produce electricity through two-electrode reactions: hydrogen oxidation (HOR) and oxygen reduction (ORR)⁵. Recent researches report that unexpected operating conditions, such as a sudden shut-down and fuel starvation, induce voltage reversal to corrode hydrogen electrodes, degrading the durability of the systems. When shut-down occurs in water electrolysis, the potential of the hydrogen electrode is increased, leading to degradation at the hydrogen electrode^{6,7}. In polymer electrolyte membrane (PEM) fuel cell operation, fuel starvation occurring at the anode side leads to a voltage reversal phenomenon, causing corrosion of carbon components like catalyst support, gas diffusion layer (GDL) and flow field plate on the anode^{8,9}. A recent study proposed to reduce the damage to the electrode by selectively promoting HOR catalysts by suppressing ORR¹⁰ and introducing a water oxidation catalyst to the anode of the PEM fuel cell to induce an OER, as it is a reaction compete with the carbon corrosion reaction⁹. In this regard, multifunctional catalysts can be a promising strategy in environments where the electrochemical reaction changes rapidly, such as the voltage reversal of water electrolysis and PEM fuel cell systems.

Among the various catalysts, Ir-based materials are excellent candidates to fit this strategy owing to their remarkable OER activity as well as good HER and HOR catalytic activity¹¹⁻¹⁴. In particular, an amorphous IrO_x surface is considered the best active site for OER^{15,16}. Based on the X-ray photoemission spectroscopy (XPS) and X-ray absorption spectroscopy (XAS), amorphous IrO_x (Ir^{IV}) exhibits a higher

oxidation state than rutile IrO_2 (Ir^{IV}) due to abundant electrophilic oxygen species (O^{III}) which makes nucleophilic attack of water, leading to enhanced OER catalytic activity¹⁷⁻¹⁹. For HER and HOR, it has been reported that metallic-Ir surfaces such as Ir (111) show significant catalytic activities^{20,21}. Thus, Ir-based materials possess good OER, HER and HOR catalytic activity and can be used as anodes and cathodes of water electrolyzer and as anodes of PEM fuel cells. However, despite the multifunctionality of Ir-based catalysts, the inconsistent active sites and irreversibility of Ir for HER, HOR, and OER have limitations in their application to real device systems with varying operating conditions. The Strasser group reported that Ir nanoparticles irreversibly changed to oxide formation under potential cycling over than $1.0 V_{\text{RHE}}$ ¹⁴. Fuel starvation in PEM fuel cells or voltage reversal in water electrolysis occurs, irreversible oxidation of Ir-based catalyst would happen at the anode in the fuel cell and at the cathode in water electrolyzers, resulting in the loss of multifunctional catalytic properties. Therefore, securing the reversible properties of Ir nanoparticles can be a viable alternative that can improve the durability of fuel cells and water electrolysis systems while maintaining multifunctional catalytic properties.

Herein, we introduce a crystalline Ir-based alloy catalyst as a strategy to maintain the electrochemical reversibility of Ir. Alloying Ir with a transition metal is an efficient method to improve the kinetics of OER, HER and HOR^{22,23}. We synthesized carbon-supported IrNi alloy nanoparticles with high crystallinity (IrNi/C-HT) and with low crystallinity (IrNi/C-LT), both of which exhibited excellent OER/HER/HOR catalytic activity. Based on the results of *in situ/operando* X-ray absorption near edge structure (XANES) and depth-resolved XPS, HER and HOR performance of IrNi/C-LT sharply decreased after the OER measurement, due to conversion of the irreversible amorphous IrNiO_x surface. However, IrNi/C-HT possesses a very thin IrNiO_x layer under the OER condition and this IrNiO_x layer is reversibly converted to a metallic surface under the HER condition, exhibiting high HER performance. We explored the mechanism of the reversible IrNiO_x layer of IrNi/C-HT using electrochemical flow-cell coupling *operando* inductively coupled plasma-mass spectrometry (ICP-MS). In addition, the prepared catalysts were applied to the fuel starvation of the PEM fuel cell and the reverse voltage of the water electrolyzer to confirm their viability in a real environment.

Results

IrNi/C morphology and crystallinity: synthesis temperature

IrNi nanoparticles supported on carbon (IrNi/C) were synthesized using a modified impregnation method that instantly changed to reductive gas conditions at target heat-treatment temperatures, in order to control the crystallinity while maintaining a small particle size. Synthesized IrNi/C materials treated at 400 °C and 1000 °C were denoted as IrNi/C-LT and IrNi/C-HT, respectively. For comparison, Ir/C-LT and Ir/C-HT were prepared by the same method without the nickel precursor. The high-resolution transmission electron microscopy (HR-TEM) images of IrNi/C-LT and -HT (Figs. 1a and 1d) show a similar particle size (1–1.5 nm) and distribution. Energy-dispersive X-ray (EDX) mapping images of IrNi/C catalysts (**Supplementary Fig. 1**) reveal that Ir and Ni are homogeneously distributed on the carbon support in

atomic proximity suggesting the presence of an Ir and Ni alloy. Based on the TEM EDX images (**Supplementary Fig. 2**), the atomic ratios of Ir:Ni were 78:21 and 66:34 for IrNi/C-LT and IrNi/C-HT, respectively. However, as shown in the high-angle annular dark field (HAADF) image (Figs. 1b, 1c, 1e, and 1f), IrNi/C-LT showed a polycrystalline and amorphous structure with low crystallinity, whereas IrNi/C-HT displayed an almost single crystal character with high crystallinity. IrNi/C-HT nanoparticles exhibited (111) and (200) facets, suggesting [011] FCC single-crystal structure. The above crystallinity differences were confirmed by X-ray diffraction (XRD) (**Supplementary Fig. 3**). The (111) reflection of IrNi/C-HT was located at 41.1° , upshifted relative to that of metallic Ir at 40.6° (see JCPDS no. 87-0715), suggesting a disordered Ir-Ni alloy. In contrast, an Ir alloy peak was not observed for IrNi/C-LT due to its small particle size and low crystallinity. Sharp XRD reflections as well as HR-TEM images confirmed the presence of few large Ni particles (**Supplementary Fig. 4**). A similar relation between temperature and crystallinity at comparable particle size was observed for the pure Ir/C catalysts (**Supplementary Figs. 5 and 6**). Based on these results, we concluded that a control the crystallinity of IrNi/C catalysts via annealing temperature at comparable 1 ~ 2 nm particle size and alloy atomic ratio was achieved. The rational reason of a small particle size with high crystallinity as described above is as follows. First, the dry product of carbon support with Ir and Ni precursor containing solution leads that Ir and Ni ions attach to the carbon support in atomic-scale fine dispersion. These are hardly reduced in N_2 without H_2 gas even at high temperatures. This prevents Ostwald ripening/agglomeration during thermal treatments of up to $1000^\circ C$. Second, when the N_2 gas was immediately changed to 10% H_2 (99.999%) and 90% N_2 at $1000^\circ C$, reduction occurred quickly, leading higher nucleation density and a finer nuclei size. This effect can be inferred from conventional nucleation theory²⁴. When the temperature is raised with an H_2 atmosphere, the reduction proceeds slowly due to a low temperature. This leads to Ostwald ripening acceleration, resulting that the particle size is not finer, as shown in **Supplementary Fig. 7**. In that state, only the IrNi/C-HT sample undergoes a sufficient crystallization step to form single-crystal nanoparticles with high crystallinity.

Electrochemical properties and catalytic activity

To investigate the effect of crystallinity on the electrochemical properties, the cyclic voltammetry (CV) of the prepared IrNi/C-LT and IrNi/C-HT was measured under changing upper potential limits (UPL), (**Figures 2a and 2b**). As the UPL increased during the CV of IrNi/C-LT, the hydrogen adsorption-desorption (H_{upd}) peak associated with a metallic Ir surface disappeared and two redox peaks associated with Ir(III)/Ir(IV) and Ir(IV)/Ir(>IV) emerged²⁵. When the UPL was decreased, the CV shape of IrNi/C-LT was maintained. This indicated that the surface of the IrNi/C-LT irreversibly changed from a metallic-IrNi alloy to $IrNiO_x$. In contrast, the H_{upd} peak area of IrNi/C-HT decreased with increasing UPL but restored again as the UPL decreased. These findings suggested that the surface of IrNi/C-HT reversibly converted between a metallic character and an oxidic $IrNiO_x$ character. Again, a similar behavior was obvious for pure Ir/C (**Supplementary Figure 8**).

Figure 2c demonstrate the electrocatalytic performance of the catalysts during a set of subsequent linear voltammetric scans probing first the HER, then the OER, and then again the HER reactivity, all in 0.05 M H_2SO_4 . Prior to the OER test, the catalysts were activated by 50 CV cycles to generate an IrO_x layer.

Compared with Ir/C catalysts, IrNi/C catalysts demonstrated higher HER catalytic activity, comparable with commercial Pt/C. Ir/C-LT demonstrated a more enhanced OER performance compared to Ir/C-HT, due to the large amount of redox active Ir centers represented by the redox charge (**Figures 2a** and **2b**). The Ir-Ni alloys generally show a superior catalytic activity for the OER, regardless of their crystallinity. To evaluate metal-oxide reversibility, HER performances were re-measured after the OER test. While the IrNi/C-HT catalyst maintained high HER reactivity, that of the IrNi/C-LT catalyst decreased. These distinctly different levels of reversibility are reflected by the HER overpotentials (**Figure 2d**) and the Tafel plots (**Supplementary Figure 9**), as well. Interestingly, the analogous behavioral trends were observed in the HOR/OER reversibility (**Figures 2e** and **2f**): Initial HOR performance of IrNi/C catalysts is comparable with the commercial Pt/C catalyst. After 10 CV cycles, the HOR catalytic activity of IrNi/C-LT dropped markedly, but that of IrNi/C-HT decreased only slightly. These results evidence that Ir-based nanocatalysts with high crystallinity show a remarkable reversibility in their surface electrochemistry and their associated electrocatalytic reactivity for oxidation and reduction reactions, such as HER/OER and HOR/OER.

To explain the reversible character of the IrNi/C-HT, we tracked the electronic structure and oxide thickness of IrNi@IrNiO_x core-shell nanoparticles under intermittent OER and HER operating conditions using *in situ/operando* X-ray absorption near-edge structure (XANES), which was measured at the Ir L₃-edge to probe electron transitions from 2p to 5d. Since XANES is a bulk sensitivity technique, it is difficult to show the oxidation state of local structures. The white line of core-shell Ir nanoparticles represents the overall d-hole character, which is the redox state of both the oxidized Ir in the shell and that of the metallic Ir in the core. If the core of the catalyst state is fixed to metallic-Ir, the white-line position of the core-shell catalyst roughly represents the *d*-band hole count of Ir in the shell (**Figure 3a**)²⁶. Moreover, if the particle size is the same, the oxide thickness of the core-shell can be roughly estimated by the white-line area (**Figure 3b**).

The white-line peak positions in the experimental sequence are illustrated in **Figure 3a**. Under the OER condition, the white-line position of both IrNi/C catalysts is positively shifted with a *d*-band hole count of 5.4 compared with the Ir/C catalyst (*d*-band hole count of 5.2), as shown in **Figure 3c**. The *d*-band hole count was calculated by white-line position and formal *d*-band hole count function (**Supplementary Figure 10**). The large number of vacancies in IrNiO_x/C enhances the electrophilic character of oxygen, resulting in smaller kinetic barriers for OER²⁶⁻²⁸. These XANES results can explain the high activity of IrNi/C catalysts for OER. After OER and OER-HER operations, IrNi/C-LT has a higher white-line position than IrNi/C-HT, indicating a higher oxidation state of IrNi/C-LT after reaction. However, under HER condition, the white-line position of IrNi/C-HT is higher than that of IrNi/C-LT (**Figure 3d**). To explain this phenomenon, we estimated the chemical state of the catalyst under HER conditions. The HER Tafel slope of IrNi/C-HT (43 mV dec⁻¹) indicates that the Heyrovsky step in the Volmer-Heyrovsky mechanism is the rate determining step for IrNi/C-HT²⁹. Adsorbed hydrogen (H_{ads}) coverage is expected to be 0.25–0.50 for the Heyrovsky step³⁰. Based on previous research, H_{ads} increases the *d*-band hole count^{31,32}. Thus, H_{ads} coverage of IrNi/C-HT would slightly increase the white-line position during the HER. For IrNi/C-LT, it

is assumed that the IrO_x surface adsorbs protons at a cathodic potential and converts to an $\text{Ir}(\text{O}_x\text{H}_y)$ species which possesses a lower d -band hole count than IrO_x ^{33,34}.

To observe the oxide thickness under OER/HER operating conditions, white-line areas were identified by *in situ/operando* XANES. In all conditions, IrNi/C-HT catalysts showed smaller white-line areas than IrNi/C-LT catalysts, implying that IrNi/C-HT possesses a thinner IrO_x layer than IrNi/C-LT during OER and HER (**Figure 3b**). In particular, the IrNi/C-HT catalyst showed a highly reduced white-line area under the HER condition (**Figure 3d**), which is close to the metallic-Ir foil. Thus, IrNi/C-HT nanoparticles possess an almost metallic surface under the HER condition, leading to high HER activity. The white-line area clearly exhibits the difference between IrNi/C-HT and IrNi/C-LT under OER and HER condition. It suggests that oxide thickness is a key controlling factor of the reversibility phenomenon of IrNi@IrNiO_x core-shell nanoparticles with high crystallinity.

To study the effect of the crystallinity on the surface electronic structure in more detail, we analyzed a depth-resolved Ir 4f XPS spectra using two different levels of kinetic energy (KE). The associated inelastic mean free path associated with KEs of 210 eV and 550 eV are almost 0.5 and 0.9 nm, respectively, which represent the atomic shell layers of 2 and 3–4 Ir atoms, respectively ³⁵. The Ir 4f spectrum can be deconvoluted into the three types of Ir species: Ir⁰ (metallic-Ir), Ir[□] (rutile-type Ir[□]O^{□-}₂), and Ir[□] (amorphous Ir[□]O[□]₃) ¹⁹. The details of the deconvoluted XPS results are shown in **Supplementary Table 1**. The Ir depth profile of pristine IrNi/C electrodes indicates that the majority of nanoparticles were in the metallic state with soft oxidation of the surface (**Supplementary Figure 13**). After OER, the spectrum of the IrNi/C-LT catalyst at 210 eV KE is fully shifted to the position of the 100% Ir[□] species (**Figure 4a**). The Ir 4f line shape of the IrNi/C-LT catalyst at 550 eV KE is a mixture 53.2% Ir[□] and 46.8% Ir[□] with no metallic species, suggesting that the surface of IrNi/C-LT is completely changed to a thick amorphous IrNiO_x layer. This thick amorphous IrNiO_x shell of IrNi/C-LT is conserved after the HER condition, revealing an irreversible Ir oxide layer on IrNi/C-LT. Meanwhile, the composition of the IrNi/C-HT catalyst after OER is 69.6% Ir[□] and 30.4% Ir[□] at 210 eV KE and 39.4% Ir[□], 26.8% Ir[□], and 39.4% Ir⁰ at 550 eV KE (**Figure 4b**), indicating that an extremely thin IrNiO_x layer has been synthesized on the metallic subsurface. After HER, the ratio of Ir[□] species at 210 eV KE is significantly decreased and 38.2% metallic-Ir is observed, demonstrating that some of the thin IrNiO_x layer was turned into the metallic surface. The Ir depth profile of IrNi/C-LT and IrNi/C-HT summarized in **Figure 4c**, clearly demonstrates that the thick IrNiO_x layer of IrNi/C-LT synthesized by OER is maintained after HER and that the thin IrNiO_x layer of IrNi/C-HT converts to metallic-Ir after HER.

The description of phenomena related to crystallinity and HER/HOR/OER reversibility are illustrated in **Figure 4d**. IrNi/C-LT having low crystallinity exhibits an abundant grain boundary, which accelerates the penetration of ions into nanoparticles and results in the formation of a thick IrNiO_x layer ³⁶. *Ex-situ* HAADF and EDS mapping images shows that IrNi/C-LT (**Supplementary Figure 14**) consists of a thick amorphous IrNiO_x. This thick irreversible IrNiO_x demonstrates excellent performance for OER but poor

performance for HER and HOR. On the other hand, IrNi/C-HT with high crystallinity has no grain boundary defects, enabling formation of the very thin IrNiO_x layer. Ni of IrNi/C-HT still located with the Ir, confirming the core of the metallic structure (**Supplementary Figure 14**). This thin IrNiO_x of IrNi/C-HT is reversibly converted to a metallic structure under HER/HOR conditions, showing high reversibility for OER/HER/HOR.

Mechanism study of reversible catalytic activity

To clarify the reversible reactivity character of Ir-Ni/HT further, we correlated it to surface dissolution processes at the atomic scale and were able to uncover the underlying mechanism that leads to reversibility. To achieve this, we conducted *in situ/operando* ICP technique using an electrochemical flow cell³⁷. It is well known that electrochemically prepared IrO_x is irreversibly oxidized³⁸⁻⁴¹. Hence, there is a need for a mechanism study on the cause of reversible conversion of the IrNiO_x layer on IrNi/C-HT to a metallic surface. When cycling between 0.05 and 1.5 V_{RHE} to produce IrNiO_x species on nanoparticles, IrNi/C-LT has a large peak compared to IrNi/C-HT, indicating that IrNi/C-LT possesses a large amount of amorphous IrNiO_x. Subsequently, three types of peaks were observed.

First, the peaks of OER intermediate dissolution located at the highest potential, are associated with an intermediate Ir species during OER and lattice oxygen participation (denoted as O1 ~ O3). For the peak area of dissolution during OER, IrNi/C-HT is lower than that of IrNi/C-LT owing to the thin IrNiO_x layer of IrNi/C-HT. To confirm stability of IrNi/C-HT during reaction, the dissolution profile under OER and HER conditions was conducted and is shown in **Supplementary Figure 16**. IrNi/C-HT under OER and HER conditions showed a lower Ir dissolution as compared to IrNi/C-LT, despite similar OER catalytic activity (**Figure 2c**), demonstrating high stability of IrNi/C-HT. Second, the peaks of reversible reduction dissolution (denoted as R1 and R2) which is located at close to 1.0 V_{RHE}, close to the standard potential of Ir oxidation reaction (0.926 V + 0.0591 pH), exhibited electrochemical dissolution of reversible Ir oxides. Third, the peaks of irreversible reduction dissolution (denoted as I1, I2 and I3) located at the lowest potential, representing cathodic dissolution due to irreversible Ir oxide. Both peaks indicate the cathodic dissolution of Ir oxide. Interestingly, there is no peak of reversible reduction dissolution for IrNi/C-LT, and IrNi/C-HT after 1.3 V. When the upper potential was increased from 1.3 to 1.5 V_{RHE}, a peak of reversible reduction dissolution was observed, indicating the production of reversible Ir oxides during the OER⁴⁰. For the IrNi/C-HT, cathodic dissolution is significantly lower than that of IrNi/C-LT, indicating that metallic surface of IrNi/C-HT is not derived by removal of IrNiO_x layer through dissolution.

Mayrhofer *et al.* analyzed the reduction of Ir hydroxide using the *in situ/operando* ICP technique and suggested that cathodic dissolution can be explained by dissolution and re-deposition phenomenon and/or incomplete oxide reduction^{38,39}. Based on this hypothesis, we proposed a description of the reversible oxide film of IrNi/C-HT, as shown in **Figure 5c**. The particularly small amount of cathodic dissolution of IrNi/C-HT suggests that converted IrNiO_x almost transformed to the metallic phase, and did

not dissolve into the electrolyte. IrNi/C-HT has thin IrNiO_x layer, resulting in a metallic surface after dissolution of IrNiO_x. The adsorbed hydrogen (H_{ads}) on the metallic surface can serve to promote Ir reduction to metal⁴²⁻⁴⁴. Based on the Tafel slope, the H_{ads} coverage expected to be 0.25 ~ 0.50 during HER is sufficient for metal reductions. This metallic surface of IrNi/C-HT served as a substrate for deposition of dissolved Ir ion to accelerate the reduction of Ir ions to metallic-Ir, which supports the reversible property of IrNi/C-HT. For IrNi/C-LT, the thick oxide layer is retained despite cathodic dissolution. The IrNi/C-LT surface may have an IrO_xH_y phase under HER condition, leading to re-deposition of dissolved Ir ions and non-complete reduction of the oxide. Markovic *et al.* reported that dissolution/re-deposition phenomena can be measured by the amount of dissolution with different sweep rate⁴⁵. Fast scan rates prevent dissolved ion from diffusion layer to bulk electrolyte, leading to a lower amount of dissolved ion. Thus, a high dissolution amount ratio of slow/fast scan rate exhibits enhanced dissolution/re-deposition property. The dissolution amount ratio of slow/fast scan rate of IrNi/C-HT between 0 and 1.5 V_{RHE} is 0.310, which is higher than 0.233 for IrNi/C-LT. This result indicates that IrNi/C-HT has a dominant dissolution/re-deposition mechanism due to the metallic subsurface acting as a substrate for reduction.

Harnessing catalytic reversibility in a large-scale single PEM fuel cell.

To apply and harness the catalytic reversibility of Ir-Ni alloy nanoparticles with respect to the HOR and OER in a real electrochemical device, fuel starvation experiments were conducted in a single PEM fuel cell that was built using Ir-Ni/C-HT and Ir-Ni/C-LT as the catalytically active component in the anode catalyst layer (**Figure 6a**). The initial fuel cell performance of IrNi/C-LT and -HT is lower than that of the commercial Pt/C catalyst due to lower HOR activity and metal composition (Supplementary **Figure 17**). For the fuel starvation experiment, supplied anode gas was converted from H₂ to Ar at a current density of 100 mA cm⁻². When H₂ was exhausted at the anode, the anode potential of the commercial Pt/C catalyst increased to 1.8 V_{RHE} for OER instead of HOR, leading to a reverse potential phenomenon. After 20 s, the anode potential once more increased to 2.4 V_{RHE} for carbon oxidation reaction (COR), as shown in **Figure 6a and Supplementary Figure 18**⁹. This reaction conversion was confirmed by *in-situ* exhaust gas analysis (Supplementary **Figure 19**). In contrast, the cell voltage of both IrNi/C cells increased and maintained at 1.4–1.5 V for OER, and no CO₂ gas was observed by *in situ* exhaust gas analysis, exhibiting that high OER activity of IrNi/C catalysts prohibits corrosion of carbon support. To observe HOR catalytic activity after fuel starvation, the fuel cell performance and impedance before and after the fuel starvation test were measured and is shown in **Figure 6b, Supplementary Figure 17, Supplementary Figure 20, and Supplementary Table 2**. The performance degradation at 0.6 V of commercial TTK Pt/C catalysts was 37.2% due to the carbon support corrosion. IrNi/C-LT reduced fuel cell performance by 26.9% despite no carbon corrosion, indicating low reversibility for HOR and OER. Conversely, the performance of IrNi/C-HT decreased slightly to 9.2%, suggesting that the reversible catalytic activity of IrNi/C-HT works well under real fuel starvation condition.

To confirm the reversibility of IrNi/C-LT and -HT for HER and OER under real device conditions, reverse voltage experiments were performed in a water electrolyzer, which was to change the cell polarity every 20 min with a constant current density of 40 mA cm^{-2} (**Figure 6c**). As shown in **Figure 6d**, both catalysts were applied with the same cell voltage of 1.65 V to obtain 40 mA cm^{-2} for the first 20 min. The cell voltage of IrNi/C-LT gradually increased whenever the polarity of the electrode was changed, but in the case of IrNi/C-HT, the cell voltage remained stable even after 10 polarity conversions. These results demonstrate that IrNi/C-HT retains bifunctional catalytic activity with reversibility to HER and OER under real device conditions. Our approach promotes the reversibility of nanocatalysts that enable a variety of electrochemical reactions, which can be used as catalysts to resist the reverse voltage in fuel cells and water electrolysis systems.

Conclusions

We designed a crystalline, multifunctional Ir alloy nano-catalyst with a remarkable reversibility in reactivity during intermittent switching between cathodic and anodic processes, such as HER/OER/HER. We studied and clarified the underlying mechanism of the reversibility at the molecular scale using a number of different *in situ/operando* analysis techniques. The key to reversibility of crystalline Ir alloy nanoparticles are extremely thin IrNiO_x layers that form under OER condition. Based on the results of *in situ/operando* XANES and depth-resolving XPS profiles, thin IrNiO_x layers of IrNi/C-HT possess an increase in the number of *d*-band holes during OER, leading to excellent OER catalytic activity. Under HER conditions, this thin IrO_x layer was reversibly converted to metallic surface, which exhibited high catalytic activity for HER. As a result, IrNi/C-HT represents a reversible catalytic activity for OER/HER/HOR. Our *in situ/operando* ICP results demonstrate that the reversible IrNiO_x layers emerge from a dissolution and re-deposition mechanism. The metallic IrNi alloy under the thin IrO_x layer of IrNi/C-HT can be a catalytic substrate for reduction-dissolved Ir ions under HER conditions. Based on our reverse voltage experiment at the water electrolysis cell and our fuel starvation experiment at the PEM fuel cell, the IrNi/C-HT catalyst exhibits high reversibility for HER/OER and HOR/OER in real device conditions. Our nano-catalyst design with high crystallinity can impart unique reversible properties to provide insight into various catalytic reactions and applications.

Method

Preparation of Electrocatalysts

The IrNi nanoparticles supported on carbon (denoted as IrNi/C) electrocatalysts were prepared through the modified impregnation method. 60 mg of Iridium nitrate (Alfa Aesar), 45 mg of nickel acetate (Sigma Aldrich) and 260 mg of Carbon black (Ketjen Black EC-300J) were ultrasonically mixed in 20 mL of de-ionized (DI) water. The mixed solution was dried under vacuum at 80 °C. The resultant powder was subjected to heat-treatment under 100% N₂ (99.999%) at a flow rate of 500 cm³/min to 400 °C, then the gas was immediately changed to 10% H₂ (99.999%) and 90% N₂. The temperature was maintained at 400

°C for 5 min under the changed gas conditions and then cooled down to room temperature. The resulting powder was washed 3 times with DI water, then filtered and dried in vacuum oven at 40 °C for 12 h. The final product was denoted as IrNi/C-LT. Crystallized IrNi supported on a carbon catalyst was prepared by varying only the heat-treatment temperature to 1000 °C, and this was denoted as IrNi/C-HT. For comparison, Ir nanoparticles supported on carbon electrocatalysts synthesized at a heat-treatment temperature of 400 °C and 1000 °C were prepared, which are denoted as Ir/C-LT and Ir/C-HT, respectively.

Materials Characterization

X-ray diffraction (XRD, PANalytical, Cu $\text{K}\alpha$ radiation) was conducted to measure crystallinity and identify the nature of the electrocatalysts. The morphology of the synthesized catalyst was measured by high-resolution transmission electron microscopy (HR-TEM) using an FEI Titan™ 80-300 TEM and an FEI Talos F200X. High-resolution scanning transmission electron microscopy (STEM) was performed by the Titan 80-300 and energy dispersive X-ray spectroscopy (EDX) was conducted by the Talos F200X. The element composition of the catalyst was analysed using inductively coupled plasma-optical emission spectrometry (ICP-OES, iCAP 7000, Thermo Fisher Scientific). The depth profile of Ir nanoparticles was characterized using depth-resolved X-ray Photoelectron Spectroscopy (XPS) at the 4-D beamline of Pohang Accelerator Laboratory (PAL), Pohang, South Korea. For XPS measurements, samples were prepared by spraying and drying the catalyst ink onto carbon paper (Sigracet 39 BC) to prepare the electrode. After OER, the electrodes were electrochemically treated in two steps. First, a cyclic voltammogram (CV) between 0.05 and 1.5 V_{RHE} was performed to oxidize the electrode for 50 cycles at a scan rate of 500 mV s^{-1} . Second, the OER proceeded for 10 min under a chronopotentiometry of 1.5 V_{RHE} . For the electrodes after HER, the previous OER-treated electrodes underwent additional chronoamperometry at $-0.2 V_{\text{RHE}}$ for 10 min.

Electrochemical Analysis

Electrochemical measurements were conducted on a VSP potentiostat (Bio-Logic) in a standard three-electrode system using a rotating disk electrode (RDE, 0.196 cm^2 , glassy carbon, Pine Instrument) as the working electrode and an Hg/Hg₂SO₄ electrode as the reference electrode. The electrochemical tests were performed in a 0.05 M H₂SO₄ aqueous solution. For the counter electrode, Pt wire was used for the OER and HOR, and a graphite rod was used for the HER. The measured potential was converted to reversible hydrogen electrode (RHE) using calibration data, which was based on the CV result under H₂ saturated 0.05 M H₂SO₄. For the RDE test, 5 mg of catalyst was dispersed in 2.49 ml isopropyl alcohol (IPA), 2.49 ml DI water, and 0.02 ml of 5 wt% Nafion™ solution (Sigma) by sonication for 20 min. The mixed solution was loaded onto the RDE electrode. The total Ir loading was fixed at 3 $\mu\text{g cm}^{-2}$. Prior to the OER test, the surface of the synthesized catalyst was oxidized using cyclic voltammetry (CV) between 0.05 and 1.5 V_{RHE} , 50 cycles at a scan rate of 500 mV s^{-1} . Ohmic resistance was measured by electrochemical impedance spectroscopy from 1000 to 0.1 Hz to compensate for iR loss.

Reverse voltage test in water electrolyzer

The water electrolysis test was conducted using a 10 cm² single-cell water electrolyzer with two symmetric electrodes as both anode and cathode. To fabricate the electrodes, the synthesized catalyst was ultrasonically mixed with 5 wt% Nafion™ ionomer in IPA for 20 min. The prepared catalyst ink was directly sprayed onto a gold-coated Ti foam (Bekaert, 2GDL12N-50) at 90 °C using a heated vacuum table. The geometric area of the electrode was 10 cm², and Ir of 0.1 mg cm⁻² was loaded onto the electrode. The prepared electrode was used simultaneously as an anode and a cathode and was separated by a Nafion 212 membrane. The prepared membrane electrode assemblies (MEA) were sandwiched between the current collectors and assembled in the home-made cell body. The polarization curves were measured at room temperature and atmospheric pressure. DI water was pumped to the anode and cathode side using a peristaltic pump. For the reverse voltage experiment, 40 mA cm⁻² was applied to the single cell, and the polarity of electrode was reversed every 20 min. The details of the experiment are described in the Supplementary Methods

Fuel starvation test in PEM fuel cell

The membrane electrode assemblies (MEA) were prepared using the catalyst-coated membrane method. To fabricate the MEA, the commercial Tanaka Kikinokogyo (TKK) 46% Pt/C catalyst was used as the cathode, and the synthesized catalysts were employed as the anode. The catalysts were ultrasonically mixed with a Nafion® solution in IPA for 20 min and sprayed directly onto a Nafion 212 membrane with 5 cm² geometric area at 90 °C using a heated vacuum table. The catalyst coated membrane was then placed in a hot press at 140 °C for 3 min. Pt loading at the cathode was 0.3 mg cm⁻² and noble metal loading at the anode was 0.1 mg cm⁻². Two Teflon gaskets were used to hold the MEA, and two gas diffusion layer (GDL) papers (Sigracet SGL 39BC) were used to diffuse the supplied gases (O₂, H₂, and Ar). The prepared gasket, GDL and MEA were stacked and applied to the single-cell polymer electrolyte membrane fuel cell (PEMFC).

The PEM fuel cell test was conducted at 75 °C at 1 atm. with fully humidified O₂ at the cathode and fully humidified H₂ at the anode. The flow rate of each gas was 150 cm³/min. For the fuel starvation experiment, the current density was applied at 100 mA cm⁻² and the anode gas was changed from H₂ to Ar to create a fuel starvation condition. The details of the experiment are described in the Supporting Information. The polarization curve and impedance were measured before and after the fuel starvation experiment. The exhausted gas at the anode during the fuel starvation experiment was analyzed using online gas chromatography mass spectrometry (GC-MS). The potential behavior under fuel starvation conditions was measured using the hydrogen reference electrode⁹.

***In situ/operando* Ir L₃-edge XANES**

In situ/operando XANES measurements of Ir L₃-edges were performed in fluorescence mode at the 1D beamline of Pohang Accelerator Laboratory (PAL), Pohang, South Korea. The XANES was measured using a custom-made electrochemical flow cell³⁷. A Pt wire and graphite rod were used as counter

electrodes for OER/HOR and HER, respectively. For the reference electrode, Ag/AgCl (3 M NaCl) was used. The working electrode was prepared by spraying catalyst ink, which is used for MEA, on carbon-coated Kapton film. The XANES spectra were collected at an angle of 45° with respect to the detector and beam line. The electrochemical measurements were performed in a 0.05 M H₂SO₄ aqueous solution. Peristaltic pumps were used to flow the electrolytes at 2 ml min⁻¹. Before the measurement of *in situ/operando* XANES during OER, the electrode was electrochemically oxidized by CV between 0.05 and 1.5 V_{RHE} at a scan rate of 500 mV s⁻¹ for 50 cycles. After oxidation, XAS was measured at 1.5 V_{RHE} for *in situ* OER and -0.2 V_{RHE} for *in situ* HER. At each step, the catalyst was stabilized 5 min before the XAS test. The acquired XANES and EXAFS data were processed using the ATHENA program. The details of the experiment are described in the Supplementary Methods.

***In situ/operando* ICP-MS measurements**

In situ/operando ICP-MS tests were conducted using a custom-made electrochemical flow cell containing a three-electrode system³⁷. An Ag/AgCl electrode (ALS Co., RE-3VT, 3M NaCl) and graphite rod were used as the reference and counter electrodes, respectively. Catalyst ink was loaded onto the glassy carbon plate as a working electrode by drop-casting a total area of 0.1 cm². During *in situ/operando* ICP-MS test, 0.05 M H₂SO₄ electrolyte was pumped with 0.8 ml min⁻¹ to the flow cell, which is also connected to an inductively coupled plasma mass spectrometer (ICP-MS). 1 ppb of Re was used as an internal standard to calibrate Ir concentration. The details of the experiment are described in Supplementary Methods.

Declarations

Author Contributions

W.H. Lee designed/conducted the experiments, analyzed the data and wrote the manuscript. Y. J. Ko contributed to the HR-TEM analysis. J. H. Kim and H Kim contributed to the fuel cell tests. K. H. Chae contributed to the performed the XANES/EXAFS analysis. Y. J. Hwang, C. H. Choi and B. K. Min provided an idea for the electrochemical analysis. P. Strasser and H. -S. Oh supervised the research and wrote the manuscript. All authors reviewed the manuscript.

Competing interests

The authors declare that they have no competing interests.

Acknowledgements

This work was supported by the Korea Institute of Science and Technology (KIST) institutional program and supported by “Next Generation Carbon Upcycling Project” (Project No. 2020M1A2A6079141) through the National Research Foundation (NRF) funded by the Ministry of Science and ICT, Republic of Korea. We acknowledge the Operando laboratory at KIST for *in situ/operando* ICP-MS and Advanced Analysis

Center at KIST for the TEM and XPS measurements. We wish to thank 1D XRS KIST-PAL beamline and 4D beamline for measuring the XAS and depth-resolved XPS, respectively.

References

1. Dresselhaus, M. & Thomas, I. Alternative energy technologies. *Nature* **414**, 332 (2001).
2. Turner, J. A. Sustainable hydrogen production. *Science* **305**, 972–974 (2004).
3. Carmo, M., Fritz, D. L., Mergel, J. & Stolten, D. A comprehensive review on PEM water electrolysis. *International journal of hydrogen energy* **38**, 4901–4934 (2013).
4. Wang, M., Wang, Z., Gong, X. & Guo, Z. The intensification technologies to water electrolysis for hydrogen production—a review. *Renewable and Sustainable Energy Reviews* **29**, 573–588 (2014).
5. Litster, S. & McLean, G. PEM fuel cell electrodes. *Journal of power sources* **130**, 61–76 (2004).
6. Brightman, E., Dodwell, J., van Dijk, N. & Hinds, G. In situ characterisation of PEM water electrolyzers using a novel reference electrode. *Electrochemistry Communications* **52**, 1–4 (2015).
7. Ogawa, T., Takeuchi, M. & Kajikawa, Y. Analysis of trends and emerging technologies in water electrolysis research based on a computational method: a comparison with fuel cell research. *Sustainability* **10**, 478 (2018).
8. Taniguchi, A., Akita, T., Yasuda, K. & Miyazaki, Y. Analysis of electrocatalyst degradation in PEMFC caused by cell reversal during fuel starvation. *Journal of Power Sources* **130**, 42–49 (2004).
9. Lim, K. H., Lee, W. H., Jeong, Y. & Kim, H. Analysis of Carbon Corrosion in Anode under Fuel Starvation Using On-Line Mass Spectrometry in Polymer Electrolyte Membrane Fuel Cells. *Journal of The Electrochemical Society* **164**, F1580-F1586 (2017).
10. Jung, S.-M. *et al.* Selective electrocatalysis imparted by metal–insulator transition for durability enhancement of automotive fuel cells. *Nature Catalysis* **3**, 639–684 (2020).
11. Ohyama, J., Kumada, D. & Satsuma, A. Improved hydrogen oxidation reaction under alkaline conditions by ruthenium–iridium alloyed nanoparticles. *Journal of Materials Chemistry A* **4**, 15980–15985 (2016).
12. Durst, J. *et al.* New insights into the electrochemical hydrogen oxidation and evolution reaction mechanism. *Energy & Environmental Science* **7**, 2255–2260 (2014).
13. Beni, G., Schiavone, L., Shay, J., Dautremont-Smith, W. & Schneider, B. Electrocatalytic oxygen evolution on reactively sputtered electrochromic iridium oxide films. *Nature* **282**, 281 (1979).
14. Reier, T., Oezaslan, M. & Strasser, P. Electrocatalytic oxygen evolution reaction (OER) on Ru, Ir, and Pt catalysts: a comparative study of nanoparticles and bulk materials. *Acs Catalysis* **2**, 1765–1772 (2012).
15. Willinger, E., Massué, C., Schlögl, R. & Willinger, M. G. Identifying key structural features of IrO_x water splitting catalysts. *Journal of the American Chemical Society* **139**, 12093–12101 (2017).
16. Ooka, H. *et al.* Legitimate intermediates of oxygen evolution on iridium oxide revealed by in situ electrochemical evanescent wave spectroscopy. *Physical Chemistry Chemical Physics* **18**, 15199–

- 15204 (2016).
17. Pfeifer, V. *et al.* The electronic structure of iridium oxide electrodes active in water splitting. *Physical Chemistry Chemical Physics* **18**, 2292–2296 (2016).
 18. Massué, C. *et al.* Reactive Electrophilic OI – Species Evidenced in High-Performance Iridium Oxohydroxide Water Oxidation Electrocatalysts. *ChemSusChem* **10**, 4786–4798 (2017).
 19. Pfeifer, V. *et al.* The electronic structure of iridium and its oxides. *Surface and Interface Analysis* **48**, 261–273 (2016).
 20. Strmcnik, D. *et al.* Improving the hydrogen oxidation reaction rate by promotion of hydroxyl adsorption. *Nature chemistry* **5**, 300 (2013).
 21. Kuttiyiel, K. A., Sasaki, K., Chen, W.-F., Su, D. & Adzic, R. R. Core–shell, hollow-structured iridium–nickel nitride nanoparticles for the hydrogen evolution reaction. *Journal of Materials Chemistry A* **2**, 591–594 (2014).
 22. Kutz, R. B. *et al.* Sustainion Imidazolium-Functionalized Polymers for Carbon Dioxide Electrolysis. **5**, 929–936 (2017).
 23. Feng, J. *et al.* Iridium-based multimetallic porous hollow nanocrystals for efficient overall-water-splitting catalysis. *Advanced Materials* **29**, 1703798 (2017).
 24. Karthika, S., Radhakrishnan, T. K. & Kalaichelvi, P. A Review of Classical and Nonclassical Nucleation Theories. *Crystal Growth & Design* **16**, 6663–6681, doi:10.1021/acs.cgd.6b00794 (2016).
 25. Oh, H.-S., Nong, H. N., Reier, T., Gliech, M. & Strasser, P. Oxide-supported Ir nanodendrites with high activity and durability for the oxygen evolution reaction in acid PEM water electrolyzers. *Chemical science* **6**, 3321–3328 (2015).
 26. Nong, H. N. *et al.* A unique oxygen ligand environment facilitates water oxidation in hole-doped IrNiO_x core–shell electrocatalysts. *Nature Catalysis* **1**, 841 (2018).
 27. Nong, H. N., Gan, L., Willinger, E., Teschner, D. & Strasser, P. IrO_x core-shell nanocatalysts for cost-and energy-efficient electrochemical water splitting. *Chemical Science* **5**, 2955–2963 (2014).
 28. Reier, T. *et al.* Molecular insight in structure and activity of highly efficient, low-Ir Ir–Ni oxide catalysts for electrochemical water splitting (OER). *Journal of the American Chemical Society* **137**, 13031–13040 (2015).
 29. Shi, Y. & Zhang, B. Recent advances in transition metal phosphide nanomaterials: synthesis and applications in hydrogen evolution reaction. *Chemical Society Reviews* **45**, 1529–1541 (2016).
 30. Li, Y. *et al.* MoS₂ nanoparticles grown on graphene: an advanced catalyst for the hydrogen evolution reaction. *Journal of the American Chemical Society* **133**, 7296–7299 (2011).
 31. Gorczyca, A. *et al.* Monitoring Morphology and Hydrogen Coverage of Nanometric Pt/γ-Al₂O₃ Particles by In Situ HERFD–XANES and Quantum Simulations. *Angewandte Chemie* **126**, 12634–12637 (2014).
 32. Singh, J., Nelson, R. C., Vicente, B. C., Scott, S. L. & van Bokhoven, J. A. Electronic structure of alumina-supported monometallic Pt and bimetallic PtSn catalysts under hydrogen and carbon

- monoxide environment. *Physical Chemistry Chemical Physics* **12**, 5668–5677 (2010).
33. Pedersen, A. F. *et al.* Operando XAS Study of the Surface Oxidation State on a Monolayer IrO_x on RuO_x and Ru Oxide Based Nanoparticles for Oxygen Evolution in Acidic Media. *The Journal of Physical Chemistry B* **122**, 878–887 (2018).
34. Hillman, A. R., Skopek, M. A. & Gurman, S. J. X-Ray spectroscopy of electrochemically deposited iridium oxide films: detection of multiple sites through structural disorder. *Physical Chemistry Chemical Physics* **13**, 5252–5263 (2011).
35. Tanuma, S., Powell, C. J. & Penn, D. R. Calculations of electron inelastic mean free paths. II. Data for 27 elements over the 50–2000 eV range. *Surface and Interface Analysis* **17**, 911–926 (1991).
36. Li, T. *et al.* Atomic-scale insights into surface species of electrocatalysts in three dimensions. *Nature Catalysis* **1**, 300 (2018).
37. Lee, W. H. *et al.* Carbon-Supported IrCoO_x nanoparticles as an efficient and stable OER electrocatalyst for practicable CO₂ electrolysis. *Applied Catalysis B: Environmental*, 118820 (2020).
38. Cherevko, S., Geiger, S., Kasian, O., Mingers, A. & Mayrhofer, K. J. Oxygen evolution activity and stability of iridium in acidic media. Part 1.–Metallic iridium. *Journal of Electroanalytical Chemistry* **773**, 69–78 (2016).
39. Cherevko, S., Geiger, S., Kasian, O., Mingers, A. & Mayrhofer, K. J. Oxygen evolution activity and stability of iridium in acidic media. Part 2.–Electrochemically grown hydrous iridium oxide. *Journal of Electroanalytical Chemistry* **774**, 102–110 (2016).
40. Jovanovič, P. *et al.* Electrochemical dissolution of iridium and iridium oxide particles in acidic media: transmission electron microscopy, electrochemical flow cell coupled to inductively coupled plasma mass spectrometry, and X-ray absorption spectroscopy study. *Journal of the American Chemical Society* **139**, 12837–12846 (2017).
41. Geiger, S. *et al.* The stability number as a metric for electrocatalyst stability benchmarking. *Nature Catalysis* **1**, 508 (2018).
42. El Sawy, E. N. & Birss, V. I. Nano-porous iridium and iridium oxide thin films formed by high efficiency electrodeposition. *Journal of Materials Chemistry* **19**, 8244–8252 (2009).
43. El Sawy, E. N. & Birss, V. I. A comparative study of the electrodeposition of nanoporous Ir and Pt thin films. *Journal of The Electrochemical Society* **160**, D386-D393 (2013).
44. Le Vot, S., Roué, L. & Bélanger, D. Electrodeposition of iridium onto glassy carbon and platinum electrodes. *Electrochimica Acta* **59**, 49–56 (2012).
45. Lopes, P. P. *et al.* Dynamics of electrochemical Pt dissolution at atomic and molecular levels. *Journal of Electroanalytical Chemistry* **819**, 123–129 (2018).

Figures

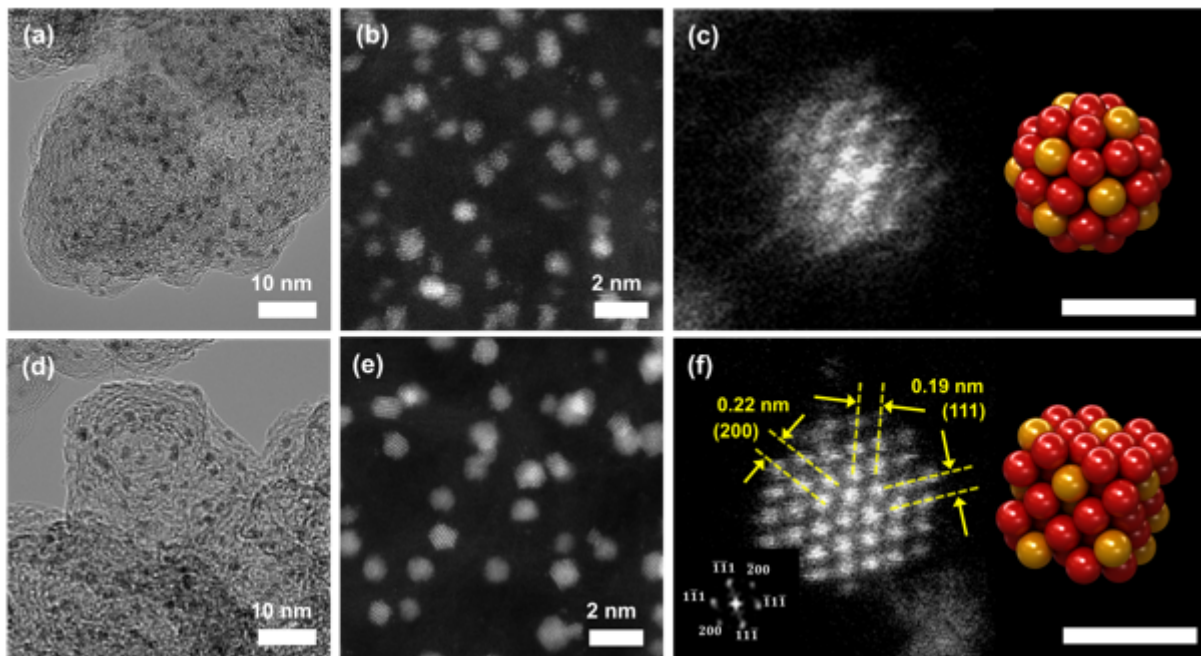


Figure 1

Morphological and structural characteristics of the synthesized IrNi nanoparticles supported on carbon at different heat-treatment temperatures of 400 °C and 1000 °C, which are denoted as IrNi/C-LT and IrNi/C-HT, respectively. (a) TEM and (b, c) HADDF images of IrNi/C-LT. (d) TEM and (e, f) HADDF images of IrNi/C-HT. The inserted fast Fourier transform of the IrNi/C-HT particles showing the (111) and (200) planes. The scale bars of Figure 1c and 1f are both 1 nm.

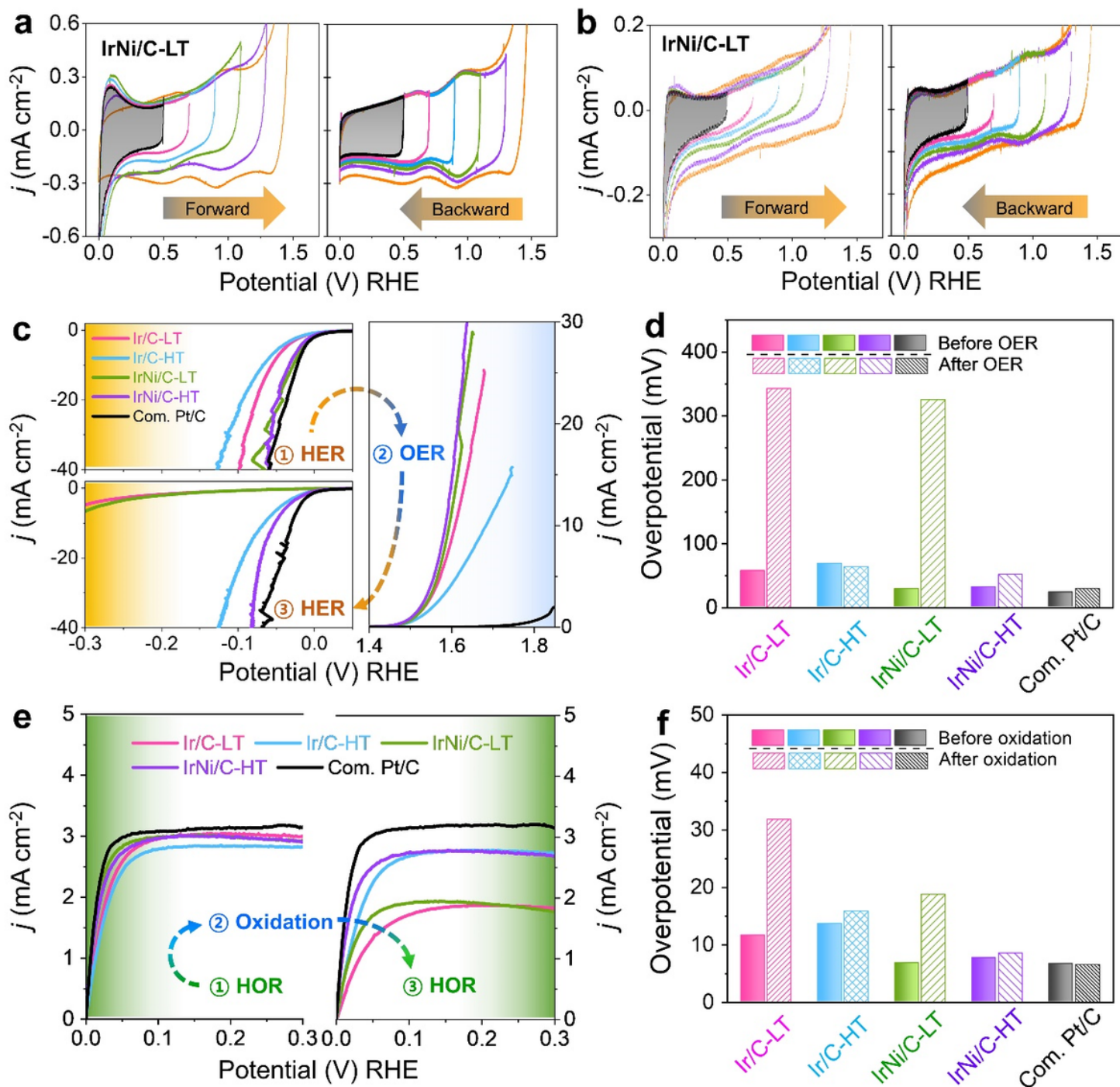


Figure 2

Electrochemical property and catalytic reversibility of the Ir-based electrocatalyst. Cyclic voltammetry (CV) of (a) IrNi/C-LT and (b) IrNi/C-HT catalyst recorded with 50 mV s⁻¹ in 0.05 M H₂SO₄ solution. The lower potential limit (LPL) is constantly 0.05 VRHE. The upper potential limit was increased from 0.5 to 1.5 V and decreased from 1.5 to 0.5 V in 200-mV steps. (c) iR-corrected current-potential curves for HER, OER, and HER after OER. (d) Comparison between trends in activities for HER and HER after OER test, expressed as overpotentials required for 10 mA cm⁻². (e) iR-corrected current-potential curves for HOR and HOR after oxidation. Oxidation was conducted by five cycles of CV between 0.05 and 1.5 V. (f)

Comparison between trends in activities for HOR and HOR after oxidation, expressed as overpotentials required for 1 mA cm⁻².

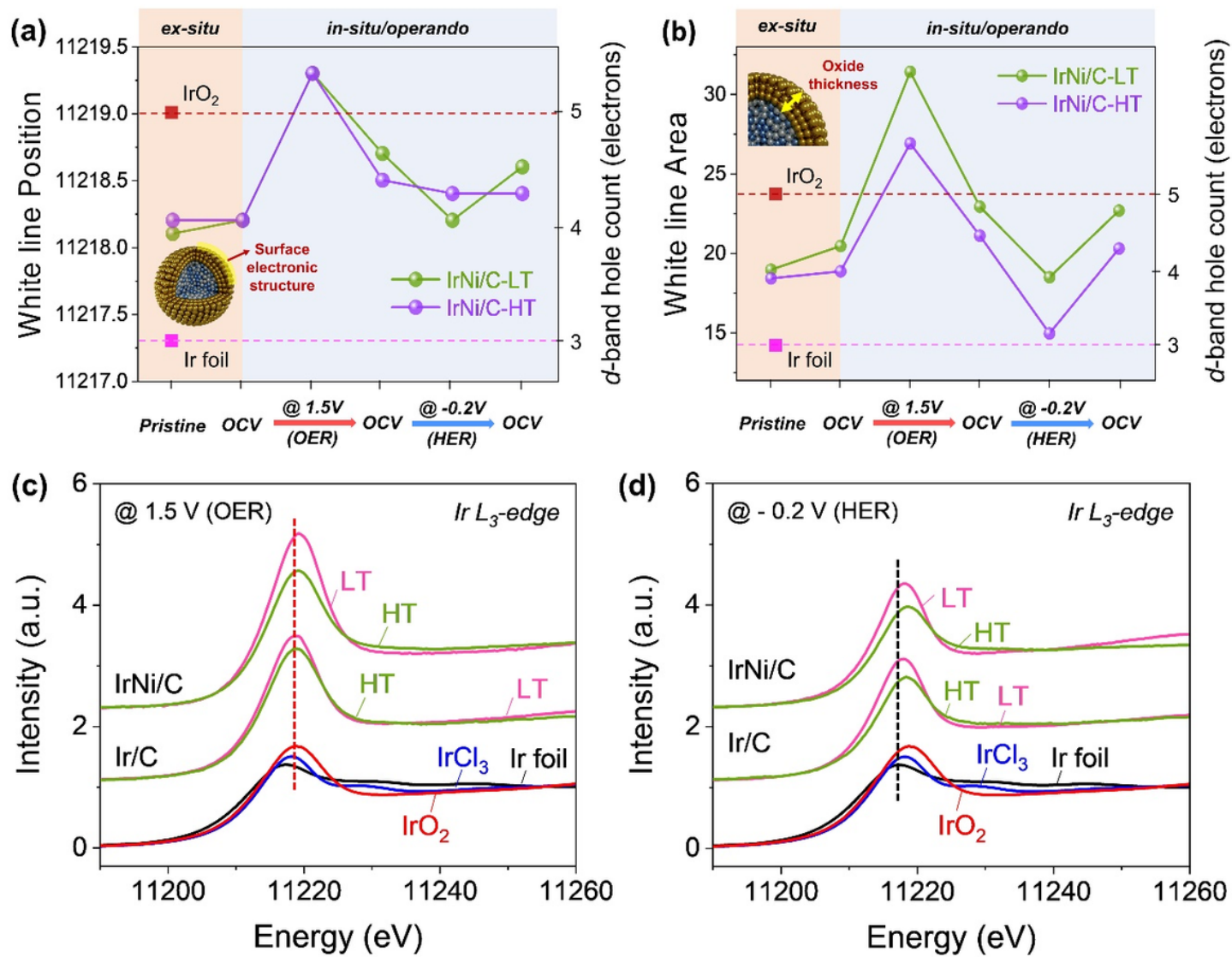


Figure 3

In situ/operando study of Ir-based electrocatalysts for electronic structure and oxide thickness analysis. Ir L₃-edge XANES of synthesized catalysts measured under experimental sequence: (i) pristine electrocatalysts powder, (ii) spray coated on electrode in 0.05 M H₂SO₄ at OCV, (iii) OER operating condition at 1.5 VRHE, (iv) OCV after OER operation, (v) HER operating condition at -0.2 VRHE, (vi) OCV after HER operation. (a) The white-line peak position and (b) area of IrNi/C-LT and IrNi/C-HT are illustrated. Commercial Ir black and IrO₂ are measured as references under same conditions. Ir L₃-edge XANES spectra of synthetic catalyst during (c) OER and subsequent (d) HER conditions. XANES spectra under another experimental condition are shown in Figure S11 and S12.

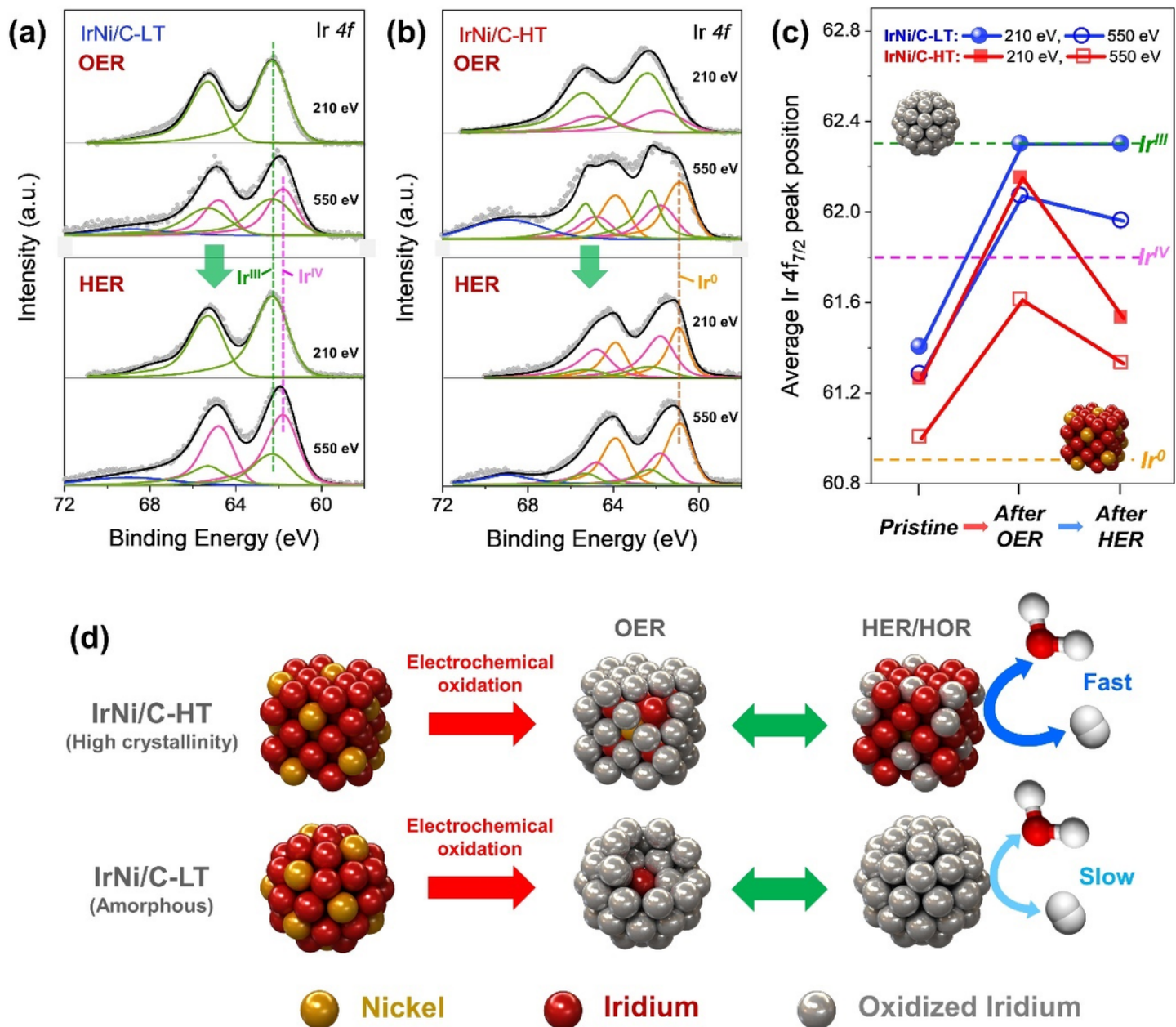


Figure 4

Surface electronic structure of Ir-based catalysts with different crystallinity. Depth-resolved Ir 4f spectrum of (a) IrNi/C-LT and (b) IrNi/C-HT after OER and followed by HER at photoelectron kinetic energies of 210 and 550 eV. (c) Average Ir 4f peak position of synthesized catalyst under experimental sequence with different photoelectron kinetic energies of 210 and 550 eV. (d) Schematic illustration of IrNi/C-LT and IrNi/C-HT under OER and HER/HOR.

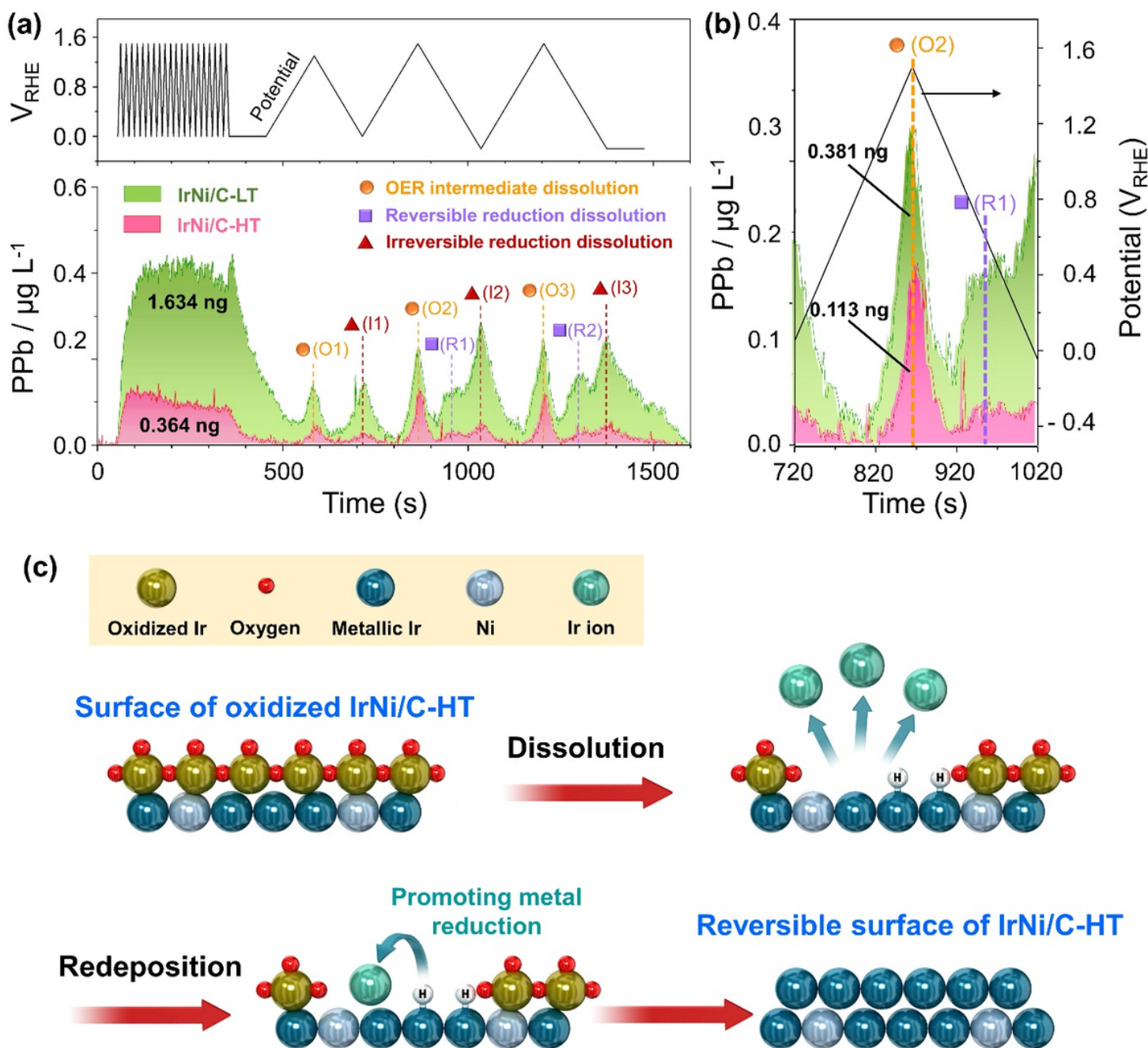


Figure 5

Mechanism study for reversible catalyst surface by in situ/operando ICP of IrNi/C-LT and IrNi/C-HT. (a) Real-time Ir dissolution profile of IrNi/C-LT and IrNi/C-HT under representative experiment sequence. (b) The Ir dissolution profile during CV in the scan range between 0 and 1.5 VRHE. (c) Reversible surface schematic of IrNi/C-HT under OER- HER conditions.

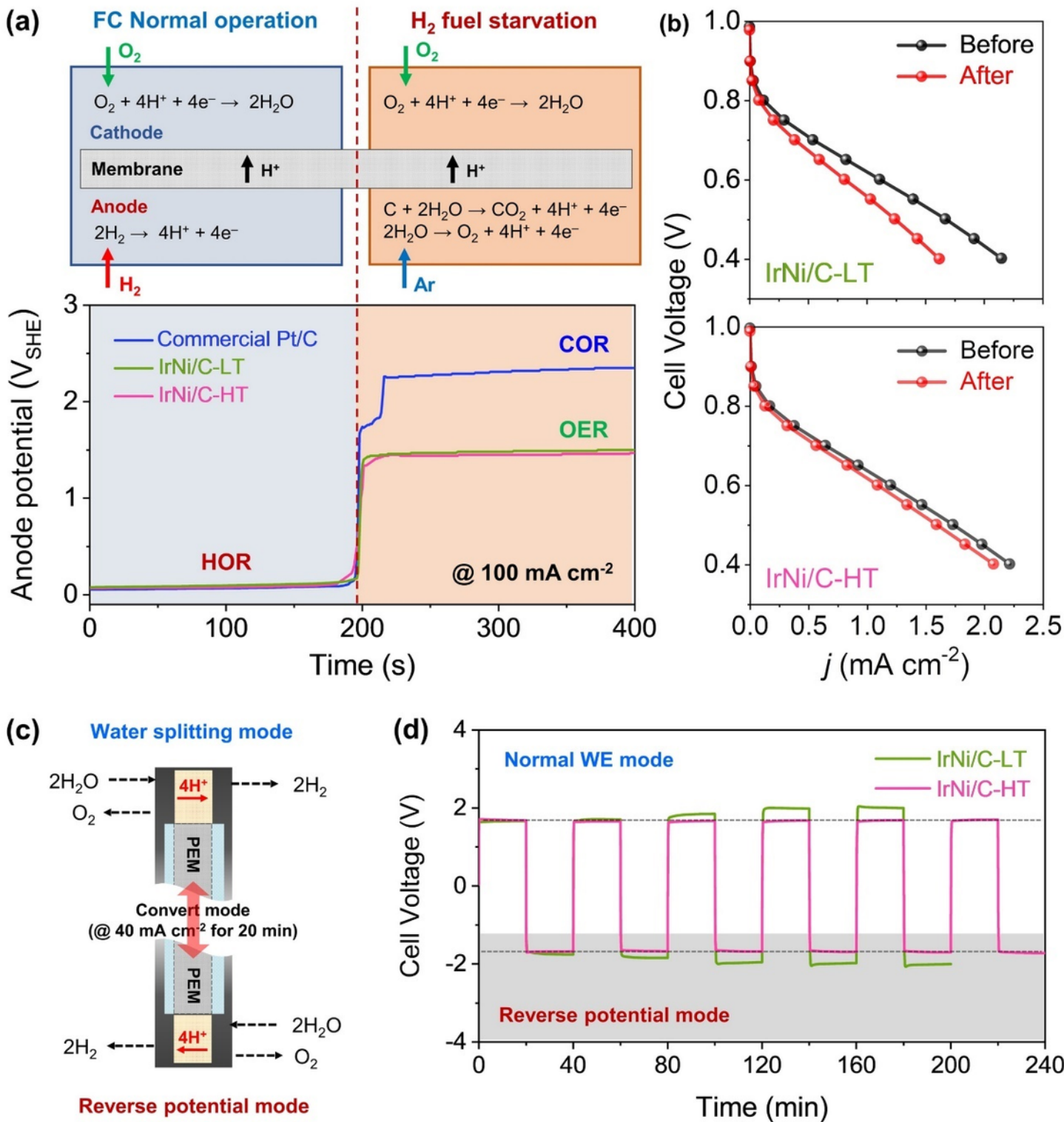


Figure 6

Reversibility of IrNi/C-HT in water electrolysis and fuel cell systems. (a) The scheme of fuel starvation experiment at fuel cell and anode potential behaviors of the commercial TTK Pt/C, IrNi/C-LT and IrNi/C-HT as the anode catalysts under the fuel starvation condition. Single fuel cell test (geometric area: 5 cm²) employing commercial TTK 46% Pt/C as the cathode. (b) Polarization curves of IrNi/C-HT and -LT before and after fuel starvation experiment. (c) The scheme of reverse voltage experiment at water

electrolyzer. (d) Reverse voltage experiment using IrNi/C-LT and IrNi/C-HT as anode and cathode of a single water electrolyzer (geometric area: 10 cm²). Galvanostatic curves obtained with current density of 40 mA cm⁻².

Supplementary Files

This is a list of supplementary files associated with this preprint. Click to download.

- [HP09reversibleIrNiCSI200826.docx](#)